Solar Energy 264 (2023) 111990

Contents lists available at ScienceDirect

Solar Energy

journal homepage: www.elsevier.com/locate/solener

Analysis of CdSe as an alternative buffer layer for Sb_2Se_3 solar cells

Narges Torabi [a], Elisa Artegiani [a], Andrea Gasparotto [b], Fabio Piccinelli [c], Matteo Meneghini [b,d], Gaudenzio Meneghesso [d], Alessandro Romeo [a,*]

[a] LAPS-Laboratory for Photovoltaics and Solid State Physics, Department of Computer Science, University of Verona, Ca' Vignal 1, Strada Le Grazie 15, 37134 Verona, Italy
[b] Department of Physics and Astronomy "G. Galilei", University of Padova, Via F. Marzolo 8, 35131 Padova, Italy
[c] Department of Biotechnology, University of Verona, Ca' Vignal 1, Strada Le Grazie 15, 37134 Verona, Italy
[d] Department of Information Engineering, University of Padova, via Gradenigo 6/B, 35131 Padova, Italy

ARTICLE INFO

Keywords:
Sb_2Se_3
CdSe
Buffer layer
Thin film
Solar cells

ABSTRACT

In this work, for the first time, CdSe is applied as a buffer layer on thermally evaporated Sb2Se3-based solar cells on superstrate configuration. The influence of this buffer layer on the growth of Sb_2Se_3 and the performance of the finished devices have been analyzed and compared with the typical CdS/Sb_2Se_3 junction.

Selenium vacancies in Sb_2Se_3 thin film act as recombination centres, for this reason applying an excessive amount of Se is beneficial to the performance of the devices. In the case of the CdS/Sb_2Se_3 structure, the high concentration gradient enhances the selenium diffusion into the CdS and the sulphur diffusion into the Sb_2Se_3 resulting in an increased number of defects. The replacement of CdS with CdSe would allow us to avoid this detrimental effect.

In this work, we show that CdSe improves the external quantum efficiency in the entire light spectrum, increasing the average current density of the devices up to 2 mA/cm^2 in comparison to CdS/Sb_2Se_3. Also, the fill factor improves while the Voc slightly decreases due to the narrower band gap. Moreover, CdSe/Sb_2Se_3 samples demonstrate excellent stability under accelerated stability tests.

1. Introduction

Antimony selenide, with a band gap of 1.2 eV, is an interesting material for photovoltaic applications, due to its outstanding optoelectronic properties and its composition based on earth-abundant elements [1]. Typically, the crystals grow with a one-dimensional structure, which limits the charge carrier loss in the grain boundaries. The highest conversion efficiency reached so far is just over 10% [2] and the achievement of a 1D structure perpendicularly oriented to the substrate, which enhances the transfer of the carriers, is a critical issue in these devices [3,4]. In superstrate configuration, the buffer layer is not only crucial for charge separation and band alignment, but it influences the crystal structure of the absorber, so the choice of a suitable buffer is even more important.

CdS is widely used and it has recently allowed the above-mentioned record efficiency [2]. TiO_2 has also been successfully applied, achieving efficiencies of more than 7%, but the optimization of the layer required different steps: in the best cells a first layer is deposited by sputtering followed by the spin coating of two additional layers [5].

The post-deposition selenization of the Sb_2Se_3 layer improves the crystal quality and enhances the efficiency by compensating the deficiency of Se, which occurs during thermal evaporation and vacuum annealing [6]. But the selenium loss in the absorber is also amplified by the diffusion of Se into the CdS, driven by the concentration gradient. The substitution of CdS with CdSe would remove the sulphur diffusion issue and contributes to the Se compensation in the absorber.

Guo et al. [7] have introduced CdSe buffer layer by RF-sputtering for close-space sublimated Sb_2Se_3 with 4.5% efficiency. This paper reports that the CdSe buffer layer improves the cells' stability, because of the reduction of defects at the interface with the elimination of sulphur diffusion.

We have applied, for the first time, CdSe to cells based on vacuum-evaporated Sb_2Se_3 at low substrate temperature in superstrate configuration and we have compared the structural/electrical properties and the stability of CdSe/Sb_2Se_3 and CdS/Sb_2Se_3 cells. At first glance, CdSe leads to a good crystal structure of the absorber with the predominance

* Corresponding author.
E-mail address: alessandro.romeo@univr.it (A. Romeo).

https://doi.org/10.1016/j.solener.2023.111990
Received 20 July 2023; Accepted 31 August 2023
Available online 10 September 2023

of the (hk1) orientations. Secondary Ion Mass Spectrometry (SIMS) and X-ray diffraction (XRD) analysis indicate that even with a low absorber deposition temperature, diffusion of S in the absorber occurs when CdS is applied, which is clearly avoided with CdSe.

Despite the lower transparency due to the narrower band gap, CdSe improves the external quantum efficiency at all wavelengths, resulting in a gain in average current density of 2 mA/cm^2 compared to the CdS/Sb_2Se_3 case. Last but not least, accelerated stability tests (AST) have demonstrated remarkable stability for the CdSe-based devices compared to the CdS ones.

2. Materials and methods

2.1. Device fabrication

Sb_2Se_3 solar cells, in our laboratory, are fabricated in superstrate configuration (see Fig. 1) on a commercial fluorine doped tin oxide (FTO)/tin oxide (TO) bi-layer coated soda lime glass. Subsequently, CdS is deposited by chemical bath deposition with 200 ml of a deionized water solution containing 15 ml of cadmium acetate, 10 ml of thiourea, and 32 ml of ammonia (20 %) at a temperature of 60 °C for 16 min. Instead, CdSe is deposited by vacuum evaporation at a substrate temperature of 340 °C at a pressure of 10^{-3} Pa; different thicknesses (from 50 up to 150 nm) have been tested and the according devices have been studied, best results were given by 50 nm thick CdSe layer which is the value taken in consideration for this work.

Sb_2Se_3 is prepared by evaporation in a different vacuum chamber, by heating a special graphite crucible, with a rate of 0.15 nm/sec and at a pressure of 3 * 10^{-4} Pa [6,8]. After optimization, the absorber thickness is kept at 600 nm. Immediately after deposition, the stack is annealed at 350 °C for 30 min in the same chamber. The back contact is made by the deposition of a 30 nm-thick gold layer. The thickness of the evaporated layers has been controlled by a quartz-crystal thickness monitor.

2.2. Physical and electrical characterization

Atomic force microscopy (AFM) images are carried out by NT-MDT Solver Pro with a SiN tip of 10 nm radius. XRD spectra are acquired with a Thermo ARL X'TRA powder diffractometer (in Bragg-Brentano geometry, equipped with a Cu-anode X-ray source (Kα, λ = 1.5418 Å) and a Peltier Si (Li) cooled solid state detector).

Low-frequency micro-Raman analyses are conducted employing a He–Ne laser (λ_{exc} = 633 nm) coupled to a single-stage Raman spectrometer (Thermo Scientific DXR2) and a charge-coupled device, thermoelectrically cooled.

SIMS depth profiles are achieved on a CAMECA IMS-4f using a Cs^+ primary ion beam at a 10 kV accelerating voltage (corresponding to 5.5 keV impact energy) and detection of positive secondary ions. The transmittance of the films is analyzed with a Unicam spectrometer Type UV2-100 in the UV–visible range.

Current density–voltage (JV) characteristics are collected with a Keithley Source Meter 2420, under an AM 1.5 spectrum at 100 mW/cm^2, using a LOT Quantum Design Europe solar simulator LS0306.

The external quantum efficiency (EQE) is obtained with a commercial LOANA solar cell analysis system, calibrated with a silicon reference sample with known EQE using an incident spotlight of 1 mm × 2 mm area.

Capacitance voltage, drive level capacitance profiling, and admittance spectroscopy are performed by an HP4284A LCR. The temperature is managed by a Janis cryostat with Lakeshore 325 temperature controller in a range between 90 K and 330 K, in a vacuum of 10^{-4} Pa.

3. Analysis and discussion

3.1. Structural properties of the absorbers

The structure of the vacuum-deposited CdSe layer, studied by AFM (see Fig. 2b), is quite similar to the one of the chemical bath-deposited CdS exhibiting exactly the same roughness with a root mean square (RMS) of 22 nm.

Similarly, for the Sb_2Se_3 layers deposited on the two different buffers, the shape, and the roughness do not show very large differences, having a very near RMS roughness: 18 nm for the absorber on CdSe and 25 nm for the one on CdS.

As mentioned in the introduction, Sb_2Se_3 is an anisotropic material with a ribbon-like structure whose orientation strongly affects electronic transport. The ribbons should be preferentially perpendicularly oriented on the substrate to allow the carrier transport between back contact and junction; this requires a predominance of the (hk1) orientations. On the other hand, (hk0) reflections highlight an orientation parallel to the substrate, which hinders the carriers' transport [4]. The Sb_2Se_3 layers here present the typical peaks that are well-matched with the JCPDS card n. PDF 15 0861 irrespectively if deposited either on CdS or on CdSe (see Fig. 3), with a large predominance of orientation along the (hk1) directions for both cases.

Furthermore, Rietveld refinement [9], performed using the MAUD software [10] shows almost the same *a* and *b* lattice parameters but, on the other hand, highlights an increase in the value of the *c* lattice parameter for the CdSe case (see Table 1). Consequently, the cell volume of the Sb_2Se_3 on the CdSe results to be larger than that for the CdS buffer. Considering the smaller atomic radius of S (1.84 Å; coordination number (CN) (6)) compared to Se (1.98 Å; CN(6)) compared to Se [11], this could suggest S diffusion and consequent replacement of Se atoms by S in the absorber with a CdS/Sb_2Se_3 junction.

To have a different point of view of the structure, Raman analysis has been applied to the same samples. Raman spectra (see Fig. 4) show peaks around 153 and 191 cm^{-1} which are commonly attributed to the Sb_2Se_3 phase; in particular, the first refers to the A_{2u} mode of the Sb-Sb bond, while the latter to the A_g mode of the Sb-Se-Sb mode. The peaks at 42 and 54 cm^{-1} have been previously detected for the first time in our Sb_2Se_3 by evaporation, and they have been attributed to strong Sb-Se modes [12]. The Raman modes at 102 and 128 cm^{-1} are typically

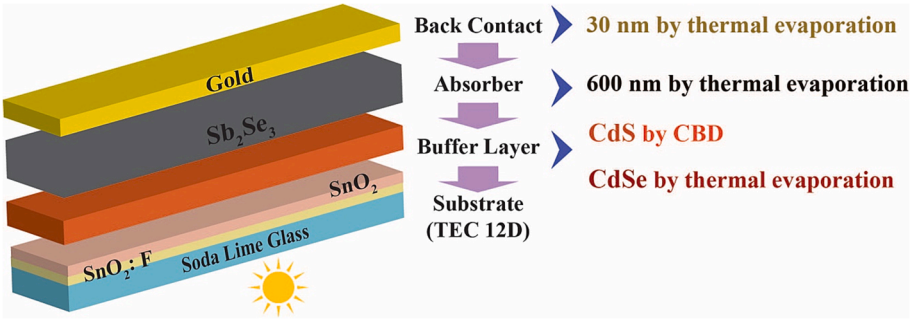

Fig. 1. Schematic structure of our Sb_2Se_3-based solar cells.

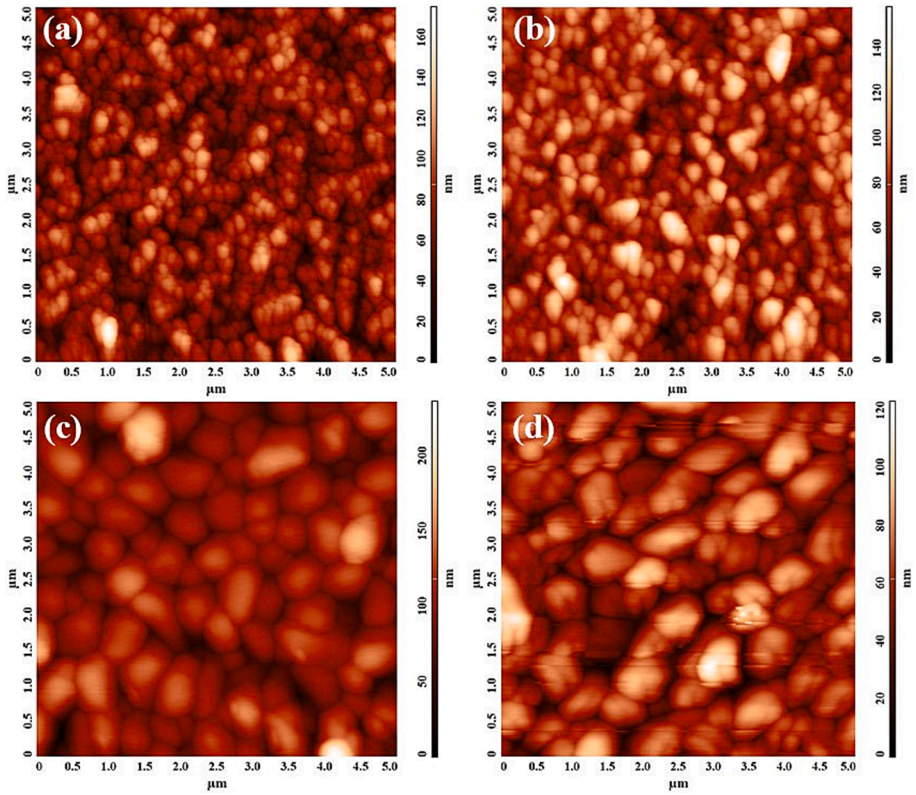

Fig. 2. AFM images of CdS (a), CdSe (b), Sb_2Se_3 deposited on CdS (c), and Sb_2Se_3 on CdSe (d).

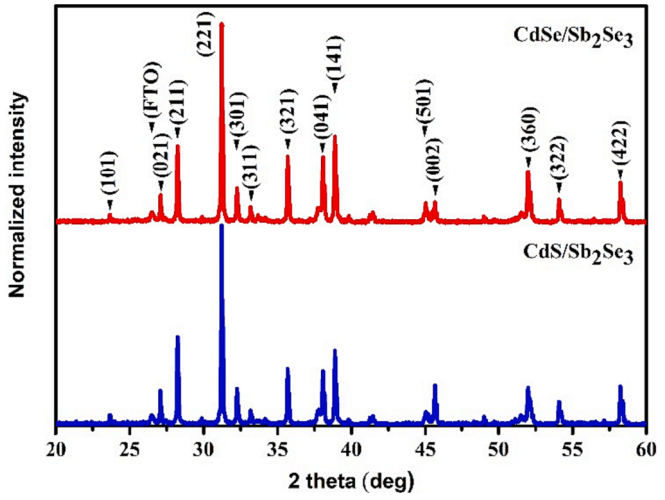

Fig. 3. XRD patterns of Sb_2Se_3 deposited on CdSe (top) and CdS (bottom).

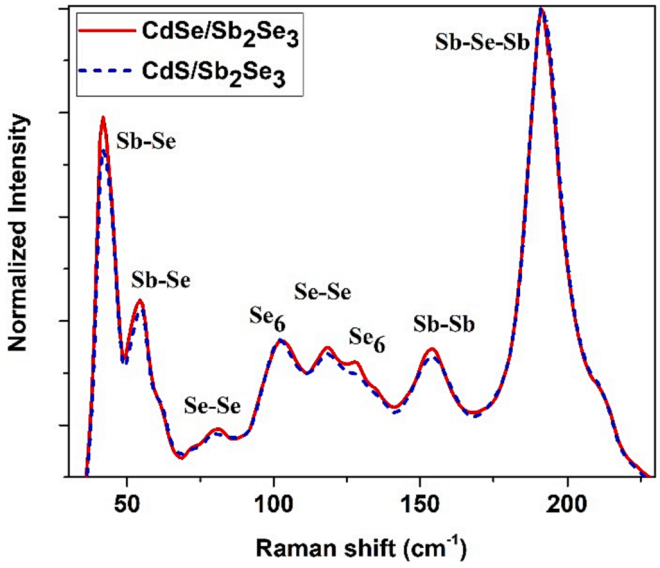

Fig. 4. Raman spectra of Sb_2Se_3 deposited on CdSe and CdS.

Table 1
Lattice parameters of Sb_2Se_3 deposited on CdSe and CdS.

	a [Å]	*b* [Å]	*c* [Å]	V [Å^3]
Sb_2Se_3 on CdSe	11.756	3.970	11.616	542.13
Sb_2Se_3 on CdS	11.754	3.972	11.605	541.80

assigned to the Se_6 ring of the rhombohedral Se structure, while the peaks at 81 and 118 cm^{-1} are assigned to the Se–Se bond [13].

If we relate the intensity of the peaks to the main mode of Sb_2Se_3 at 191 cm^{-1}, the peaks at 81, 118, and 128 cm^{-1} are more intense for the CdSe case; by the previous considerations, we can conclude that there is a larger presence of Se in the Sb_2Se_3 bulk for CdSe/Sb_2Se_3 devices. This corroborates (1) the hypothesis that the Se-loss in the absorber is amplified by its diffusion in the CdS, driven by the concentration gradient, and (2) that the introduction of a Se-containing buffer can strongly reduce this diffusion mechanism.

SIMS analysis was applied to identify punctually the above-suggested diffusion. In Fig. 5, Se, and S atoms (counts/second) are represented as a function of the sputtering depth from the absorber surface down to the TCO. The behaviour of the Se signal towards the junction is completely different in the two samples: in the CdSe case, the signal is tendentially constant towards the junction, in the CdS case, instead, the signal

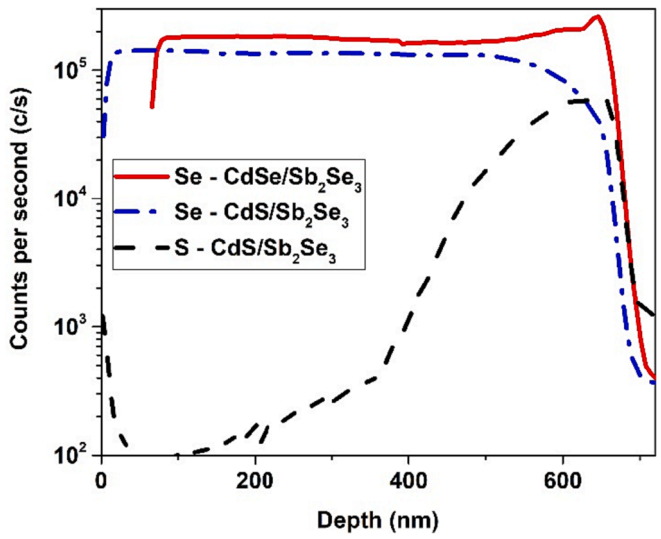

Fig. 5. SIMS depth profiles showing Se and S distribution through the absorber.

decreases in the proximity of the junction. This shows that the Sb_2Se_3 stoichiometry changes through the layer and becomes selenium poor towards the junction. Also, the Se signal is still large in the region corresponding to the S peak, where we have the CdS layer. This is an additional proof of the Se-diffusion into the CdS. On the other hand, the SIMS spectrum also shows a S-signal for at least 200–300 nm from the junction into the Sb_2Se_3, so we can also conclude that in the absorber at the proximity of the junction, we do have a mix of S-Se.

3.2. Optical and electrical characterization of the cells

Up to this point of the paper, CdSe is demonstrating interesting properties for Sb_2Se_3 devices, however, its band gap, narrower (1.7 eV) than the CdS one (2.4 eV), would foresee a reduced transparency and a reduced response in the short wavelength region of the light spectrum. This is also suggested by the transmittance spectra of CdSe and CdS buffers shown in Fig. 6: the CdSe layer shows a lower transparency in the whole range from near-UV up to near-IR.

Therefore, we would expect that with CdSe the solar cells deliver low current density. On the contrary CdSe based devices show a larger current, as shown by the JV characteristics of the cells, presented in Fig. 7, by the efficiency parameters reported in Table 2, and more significantly by the statistics on the performance parameters of the samples shown in Table 3. Average values indicate a net current gain of

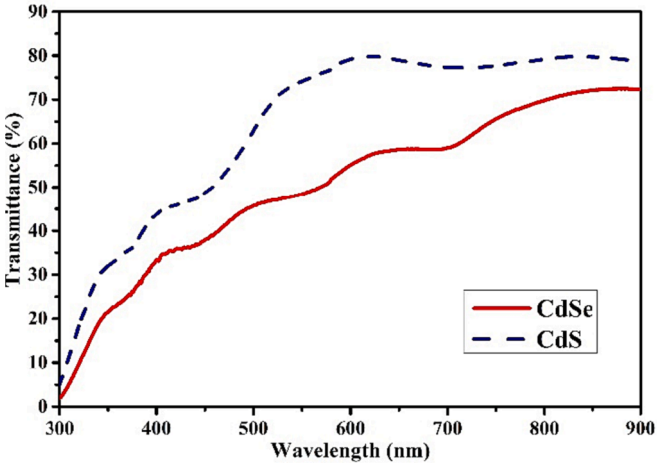

Fig. 6. Transmittance spectra of CdSe and CdS buffers.

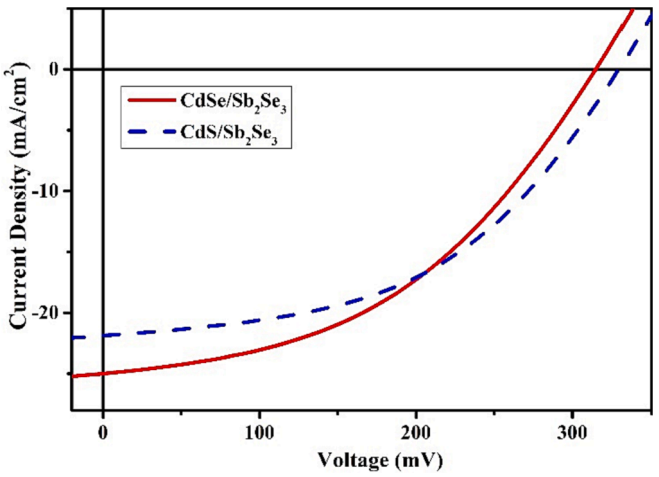

Fig. 7. J-V curves of two representative $CdSe/Sb_2Se_3$ and CdS/Sb_2Se_3 solar cells.

Table 2
Efficiency parameters of the cells presented in Fig. 7.

	FF (%)	Voc (mV)	Jsc (mA/cm^2)	Eff (%)
$CdSe/Sb_2Se_3$	43	324	25	3.5
CdS/Sb_2Se_3	47	335	21.8	3.4

Table 3
Average efficiency parameters of $CdSe/Sb_2Se_3$ and CdS/Sb_2Se_3 cells.

	FF (%)	Voc (mV)	Jsc (mA/cm^2)	Eff (%)
$CdSe/Sb_2Se_3$	44 ± 1	325 ± 5	23.7 ± 0.7	3.4 ± 0.1
CdS/Sb_2Se_3	41 ± 5	342 ± 15	21.6 ± 0.4	3.2 ± 0.2

2 mA/cm^2 for the $CdSe/Sb_2Se_3$ case. So, we have a clear improvement of the current, despite the lower band gap of the CdSe layer. This possibly suggests a lower number of defects at the junction and a consequently reduced carrier recombination.

To address this increase in current density and verify that it is effectively connected with a different device structure we have applied external quantum efficiency (EQE) shown in Fig. 8. Actually, EQE shows a larger enhancement in photon absorption of $CdSe/Sb_2Se_3$ cells across almost the entire spectrum. The lower EQE response of the CdS/Sb_2Se_3

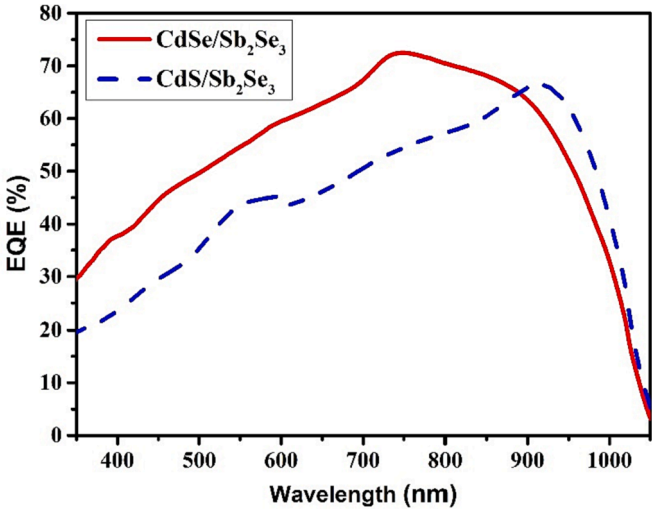

Fig. 8. Comparison of EQE of $CdSe/Sb_2Se_3$ and CdS/Sb_2Se_3 devices.

can be related to enhanced carrier recombination in the absorber, hence to a larger amount of defects (as recombination centers). Moreover, the EQE response tends to decrease with shorter wavelengths, corresponding to those photons collected in the proximity of the junction, suggesting an increasing number of defects near the buffer layer.

This is more pronounced for the CdS/Sb_2Se_3 devices, where the Se-S interdiffusion is demonstrated by the previously discussed SIMS analysis; the absence of this phenomenon in CdSe/Sb_2Se_3 devices explains the EQE gain and the consequent current density increase.

3.3. Capacitance-Voltage and admittance spectroscopy

We decided to address the defects suggested by the EQE analysis by electrical characterization of the finished devices. In Fig. 9 capacitance–voltage and drive level capacitance profiling of cells with CdS and with CdSe are shown. CV and DLCP measurements allow us to estimate the net charge density of the absorber (acceptor minus donor states) depending on the distance from the junction. The main difference between DLCP and CV is that the first is not influenced by deep defects, so by comparing the two curves we are able to identify the presence of deep states [14].

For the CdS case, see the blue dots, we have a low carrier density that explains the large depletion region (the strong rise of the profile is due to the influence of the back contact). Also, no difference between CV (open dots) and DLCP (full dots) is observed. Instead for the case of CdSe, see the red dots, the absorber shows a higher net charge density (roughly one order of magnitude higher), with a consequent narrower depletion region. In this case, a clear difference between CV and DLCP is observed, highlighting the presence of deep defects.

In order to address these possible defects, we have analysed the finished devices in terms of admittance spectroscopy and two clear defects have been identified: one level at around 400 meV (A) and the other one at 830 meV (B), see Table 4.

The first one is a deep acceptor, and it is generally attributed to either Sb vacancy [15,16] or Sb_{Se} antisite [17], while the second one can be attributed to Se_{Sb} antisite [15].

Typically the V_{Sb} at 400 meV is always present in similar analysis and it has been observed by many different laboratories (see references mentioned above), while the Se_{Sb} at 800 meV was detected by Chen et al. [15] in case of samples with Se vapor in excess over Sb. So we can

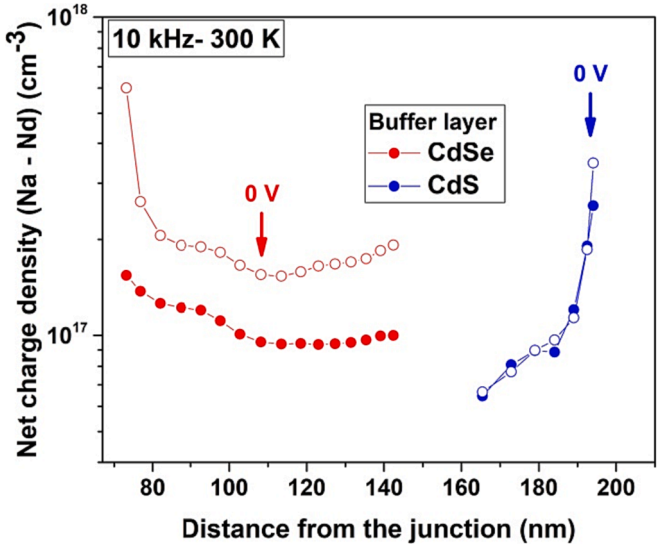

Fig. 9. CV (open dots) and DLCP (full dots) of devices with CdS (blue lines) and with CdSe (red lines) buffer layers. (For interpretation of the references to colour in this figure legend, the reader is referred to the web version of this article.)

Table 4
Defects with their respective energy and cross sections identified by admittance spectroscopy.

CdSe/Sb_2Se_3		Defect	CdS/Sb_2Se_3	
Temp.	Ea [meV]		Temp.	Ea [meV]
240 K –270 K	390 ± 6	A	270 K – 320 K	402 ± 14
320 K – 340 K	832 ± 10	B	–	–

conclude that the presence of the Se_{Sb} deep acceptor is an additional proof that for CdSe-based devices selenium loss is avoided.

3.4. Stability of the devices

Finally, we have applied accelerated stability tests by keeping the samples in a special metal chamber where a rack of halogen lamps and a temperature-controlled system maintain an illumination of around 1000 W/m^2 and a temperature of 80 °C. The cells were placed for a time of up to 1000 h and their conversion efficiency was measured periodically, as shown in Fig. 10, in order to see if the presence of sulphur in the structure would result in a long-term diffusion that could degrade the cells. For the CdSe/Sb_2Se_3 case, the values of the Voc and the current are almost constant during the AST after a rapid increase in the very first hours. For the CdS/Sb_2Se_3 case, the Voc and the Jsc show a slight reduction; on average they respectively reach 97% and 96% of the initial values after 960 h of AST.

The FF behaves differently: for the first 960 h it is much more constant with CdS than with CdSe, it decreases respectively to 96% and 87% of the initial value. FF is essentially the only parameter that leads to the degradation of the efficiency of CdSe/Sb_2Se_3 cells, while it shows an initial improvement in the first hours: probably the generated carriers fill some of the traps at the junction leading to the initial improvement, then a second phenomenon takes place.

After 960 h of testing, both devices show good stability, with attested efficiency values of 89% and 85% of the initial ones, respectively for CdS and CdSe.

Our results on degradation are in contrast with what has been reported by Guo et al. [7]. In particular, Guo's devices with CdS showed a strong instability under AST just after 120 h, with a reduction to 70 % of the initial conversion efficiency, while no degradation is reported with CdSe. The different behaviour can be explained by the different absorber deposition techniques. For Guo et al. [7] a high substrate temperature CSS deposition is used, enhancing the sulphur diffusion from the buffer to the absorber. Instead, our substrate temperature, during deposition, does not exceed 300 °C resulting in a reduced intermixing of CdS and Sb_2Se_3.

However, going longer in time, if we look at the last point reported on the graphs, corresponding to 7200 h, an evident degradation of the devices with CdS buffer layer is registered. This finally confirms that CdS enhances instability, even if for low substrate temperature deposited devices (like ours) is limited.

4. Conclusions

CdSe has been applied for the first time as an alternative buffer to Sb_2Se_3 cells on superstrate configuration fabricated by vacuum evaporation at low substrate temperature. CdSe/Sb_2Se_3 devices have been analysed and compared to the typical CdS/Sb_2Se_3 structure. The growth on CdSe leads to a flatter and more compact surface of the absorber, with a larger presence of bigger grains. XRD points out the predominance of (hk1) crystal orientations in Sb_2Se_3 deposited on both CdS and CdSe, therefore with the ribbons oriented perpendicularly on the substrate to favour the carrier transport mechanism [4]. On the other hand, Rietveld refinement reveals a smaller cell volume for Sb_2Se_3 deposited on CdS, which suggests S diffusion and consequent replacement of Se atoms by S in the absorber. Raman analysis indicates a larger presence of Se in

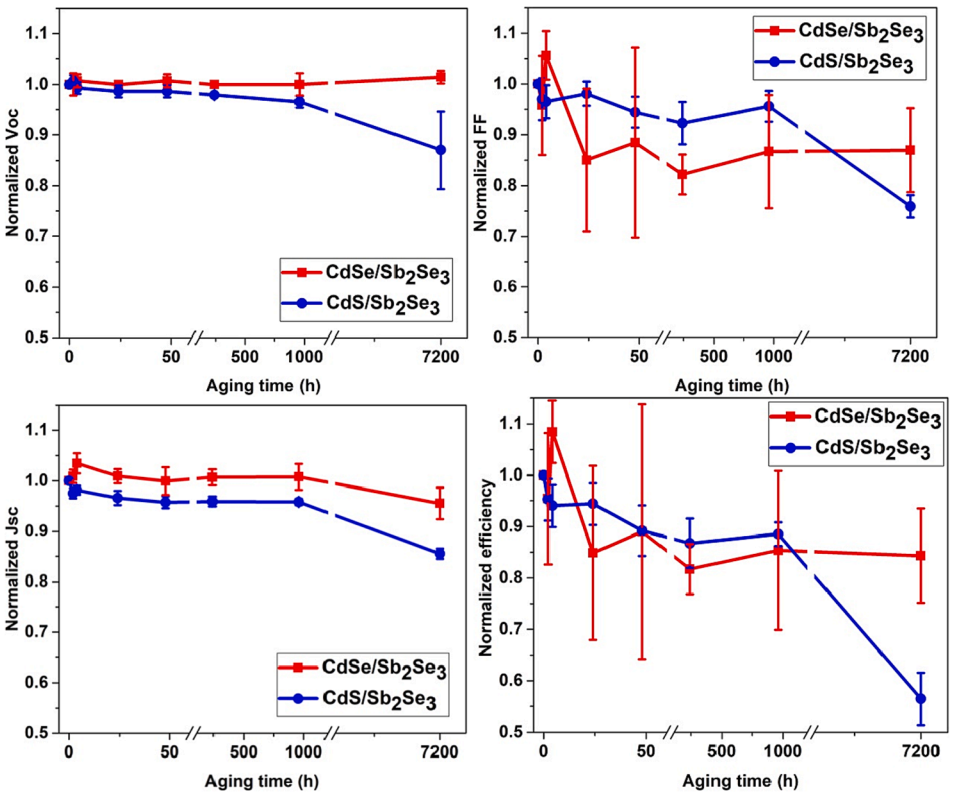

Fig. 10. V_{oc}, J_{sc}, FF and the consequent efficiency degradation versus time under accelerated stability test of $CdSe/Sb_2Se_3$ and CdS/Sb_2Se_3 samples.

Sb_2Se_3 using CdSe, supporting the hypothesis that avoiding a concentration gradient for selenium at the junction reduces the loss of Se in the absorber. Moreover, SIMS analysis clearly shows the interdiffusion of S and Se with CdS, with a deficiency of Se in Sb_2Se_3 towards the junction; while with CdSe, in the absorber the Se profile increases toward the junction.

Despite the lower transparency of CdSe, due to its narrower band gap, $CdSe/Sb_2Se_3$ cells perform at higher current densities. The FF also improves, while the Voc slightly decreases, again due to the narrower band gap compared to CdS.

The current gain is due to an increase of the quantum efficiency at all wavelengths, which can be explained by a reduction of the carrier recombination in the absorber, therefore to a reduced amount of defects, most probably related to S - Se interdiffusion.

Finally, $CdSe/Sb_2Se_3$ cells also show good stability when submitted to accelerated stability tests: after 960 h of accelerated lifetime testing, they perform 85% of the initial efficiency. A longer AST highlights a higher degradation for the CdS-based devices.

In conclusion, in this work the use of a selenium-containing buffer layer has been proved to avoid the S–Se interdiffusion, a phenomenon observed in the more widely used CdS/Sb_2Se_3 structure, therefore noticeably reducing the number of recombination centres and improving the current density.

Declaration of Competing Interest

The authors declare that they have no known competing financial interests or personal relationships that could have appeared to influence the work reported in this paper.

Acknowledgments

This work has been partially funded by Fondazione Cariverona with the project INSOBILD Ref. 2022.0094- ID 52271- CUP B33C22001760007.

The Technological Platform Center (CPT) at the University of Verona, in the person of Dr. Marco Giarola, is thankfully acknowledged for Raman measurements.

References

[1] Mavlonov, A., Razykov, T., Raziq, F., Gan, J., Chantana, J., Kawano, Y., Nishimura, T., Wei, H., Zakutayev, A., Minemoto, T., Zu, X., Li, S., Qiao, L., 2020. A review of Sb_2Se_3 photovoltaic absorber materials and thin-film solar cells. Solar Energy 201, 227–246. https://doi.org/10.1016/J.SOLENER.2020.03.009.

[2] Duan, Z., Liang, X., Feng, Y., Ma, H., Liang, B., Wang, Y., Luo, S., Wang, S., Schropp, R.E.I., Mai, Y., Li, Z., 2022. Sb_2Se_3 thin-film solar cells exceeding 10% power conversion efficiency enabled by injection vapor deposition technology. Advanced Materials 34. https://doi.org/10.1002/adma.202202969.

[3] Zeng, K., Xue, D.-J., Tang, J., 2016. Antimony selenide thin-film solar cells. Semiconductor Science and Technology 31 (6), 063001.

[4] Li, D.B., Yin, X., Grice, C.R., Guan, L., Song, Z., Wang, C., Chen, C., Li, K., Cimaroli, A.J., Awni, R.A., Zhao, D., Song, H., Tang, W., Yan, Y., Tang, J., 2018. Stable and efficient CdS/Sb_2Se_3 solar cells prepared by scalable close space sublimation. Nano Energy 49, 346–353. https://doi.org/10.1016/j.nanoen.2018.04.044.

[5] Hobson, T.D.C., Phillips, L.J., Hutter, O.S., Shiel, H., Swallow, J.E.N., Savory, C.N., Nayak, P.K., Mariotti, S., Das, B., Bowen, L., Jones, L.A.H., Featherstone, T.J., Smiles, M.J., Farnworth, M.A., Zoppi, G., Thakur, P.K., Lee, T.L., Snaith, H.J., Leighton, C., Scanlon, D.O., Dhanak, V.R., Durose, K., Veal, T.D., Major, J.D., 2020. Isotype heterojunction solar cells using n-type Sb_2Se_3 thin films. Chemistry of Materials 32, 2621–2630. https://doi.org/10.1021/acs.chemmater.0c00223.

[6] Kumar, V., Artegiani, E., Punathil, P., Bertoncello, M., Meneghini, M., Piccinelli, F., Romeo, A., 2021. Analysis of Se Co-evaporation and Post-selenization for Sb_2Se_3-Based Solar Cells. ACS Appl Energy Mater. 4 (11), 12479–12486.

[7] Guo, L., Grice, C., Zhang, B., Xing, S., Li, L., Qian, X., Yan, F., 2019. Improved stability and efficiency of $CdSe/Sb_2Se_3$ thin-film solar cells. Solar Energy 188, 586–592. https://doi.org/10.1016/j.solener.2019.06.042.

[8] Kumar, V., Artegiani, E., Kumar, A., Mariotto, G., Piccinelli, F., Romeo, A., 2019. Effects of post-deposition annealing and copper inclusion in superstrate Sb_2Se_3 based solar cells by thermal evaporation. Solar Energy 193, 452–457. https://doi.org/10.1016/j.solener.2019.09.069.

[9] P. Paufler, in: R. . Young (ed.), The Rietveld Method. International Union of Crystallography. Oxford University Press 1993. 298 p. Price £ 45.00. ISBN 0–19–855577–6, Crystal Research and Technology. 30 (1995). https://doi.org/10.1002/crat.2170300412.

[10] Lutterotti, L., 2000. Maud: a Rietveld analysis program designed for the internet and experiment integration. Acta Crystallographica. Section A 56 (s1), s54–s.
[11] Shannon, R.D., 1976. Revised effective ionic radii and systematic studies of interatomic distances in halides and chalcogenides. Acta Crystallographica. Section A 32, 751–767. https://doi.org/10.1107/S0567739476001551.
[12] Kumar, A., Kumar, V., Romeo, A., Wiemer, C., Mariotto, G., 2021. Raman Spectroscopy andIn SituXRD Probing of the Thermal Decomposition of Sb_2Se_3Thin Films. Journal of Physical Chemistry C 125, 19858–19865. https://doi.org/10.1021/acs.jpcc.1c05047.
[13] Kumar, A., Kumar, V., Romeo, A., Wiemer, C., Mariotto, G., 2021. Raman spectroscopy and in situ XRD probing of the thermal decomposition of Sb_2Se_3 thin films. Journal of Physical Chemistry C 125 (36), 19858–19865.
[14] J.T. Heath, J.D. Cohen, W.N. Shafarman, Bulk and metastable defects in CuIn 1Àx Ga x Se 2 thin films using drive-level capacitance profiling, (n.d.). https://doi.org/10.1063/1.1633982.
[15] Chen, C., Kondrotas, R., Tang, J., Wang, C., Chen, W., Wen, X., Niu, G., Gao, L., Zhao, Y., Li, K., Lu, S., Zhang, J., 2018. Vapor transport deposition of antimony selenide thin film solar cells with 7.6% efficiency. Nature Communications 9. https://doi.org/10.1038/s41467-018-04634-6.
[16] Huang, M., Xu, P., Han, D., Tang, J., Chen, S., 2019. Complicated and unconventional defect properties of the quasi-one-dimensional photovoltaic semiconductor Sb_2Se_3. ACS Applied Materials & Interfaces 11, 15564–15572. https://doi.org/10.1021/acsami.9b01220.
[17] Stoliaroff, A., Lecomte, A., Rubel, O., Jobic, S., Zhang, X.H., Latouche, C., Rocquefelte, X., 2020. Deciphering the role of key defects in Sb_2Se_3, a promising candidate for chalcogenide-based solar cells. ACS Appl Energy Mater. 3, 2496–2509. https://doi.org/10.1021/acsaem.9b02192.